Enhanced light-extraction efficiency and emission directivity in compact photonic-crystal based AlGaInP thin-films for color conversion applications

Amade Ndiaye, Ahlem Ghazouani, Christian Seassal, Emmanuel Drouard, Nicolas Olivier, Badhise Ben Bakir

Research Article | Vol. 29, No. 22 / 25 Oct 2021 / Optics Express 35965
Optics EXPRESS

Enhanced light-extraction efficiency and emission directivity in compact photonic-crystal based AlGaInP thin-films for color conversion applications

AMADE NDIAYE,[1,2] AHLEM GHAZOUANI,[1] CHRISTIAN SEASSAL,[2] EMMANUEL DROUARD,[2] NICOLAS OLIVIER,[1] AND BADHISE BEN BAKIR[1,*]

[1] *Univ. Grenoble Alpes, CEA, LETI, MINATEC campus, CEA-Grenoble, F38054 Grenoble, France*
[2] *Univ. Lyon, Institut des Nanotechnologies de Lyon-INL, UMR CNRS 5270, CNRS, Ecole Centrale de Lyon, Ecully F-69134, France*
[*] *badhise.ben-bakir@cea.fr*

Abstract: We investigated the use of photonic crystals with different opto-geometrical parameters for light extraction from AlGaInP/InGaP MQW color converters. Blue-to-red and green-to-red color conversions were demonstrated using room-temperature photoluminescence with excitation wavelengths at 405nm and 514nm. Complete, compact and highly directional light extraction was demonstrated. 3D-FDTD and a herein-developed phenomenological model derived from the standard coupled-mode theory were used to analyze the results. The highest light extraction gains were ~8 times better than unpatterned reference structures, which were paired with short extraction lengths (between 2µm and 6µm depending on the acceptance angle) and directional light emission for square lattice of nanopillars with a lattice period of 400nm. The design guidelines set in this work could pave the way for the use of inorganic MQW epi-layer color converters to achieve full color microdisplays on a single wafer.

1. Introduction

Color conversion is a key strategy for many applications in the field of optoelectronics, e.g., solid-state lighting [1–3], optical communication [4], and most recently displays [5,6]. Particularly in display applications, the material system used for efficient inorganic blue and green emission is InGaN/GaN grown on sapphire substrate, while the one used for red light emission is AlGaInP/InGaP grown on GaAs substrate [7]. Those material differences make native RGB emission on the same substrate very challenging and therefore color conversion is becoming a credible alternative, particularly for red emission [5].

Figure 1 depicts the standard color conversion process from blue (or green) to red. Most commonly, an incoming pump light from a blue (or green) light-emitting diode (LED) is absorbed by a color conversion layer (CCL), converted into red light in the active region and then extracted out of the CCL.

Therefore, a common figure of merit (FoM) to assess the efficiency of a CCL is the conversion efficiency (CE) which reads as:

$$CE = \eta_{abs} \times IQE \times LEE, \tag{1}$$

where η_{abs}, IQE and LEE respectively account for absorption efficiency of the incident pump light, internal quantum efficiency and light extraction efficiency. Various types of CCL have already been reported in the literature, particularly for blue-to-red color conversion. The most common approaches so far consist in using phosphors and most recently colloidal semiconductor quantum dots (Q-dots) pumped by blue LEDs. However, due to the low absorption of phosphors

#441116 https://doi.org/10.1364/OE.441116
Journal © 2021 Received 24 Aug 2021; revised 20 Sep 2021; accepted 26 Sep 2021; published 18 Oct 2021

Optics EXPRESS

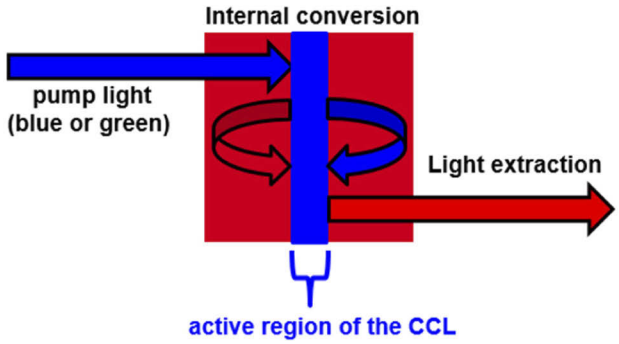

Fig. 1. Schematics depicting the color conversion process from blue (or green) to red.

and Q-dots in the blue spectral range, thick color converters are needed for complete absorption of the incident pump light as shown in Table 1. This could lead to aspect ratio issues in microdisplay applications where the lateral sizes of pixels can be less than 5 μm [11]. Besides, both strategies suffer from photostability issues which make them incompatible with applications requiring high luminances (see Table 1).

In this regard, inorganic MQW semiconductor color converters could therefore gain a lot of ground as photo-pumped color converters for an underlying blue or green emitter. Particularly, InGaP and AlGaInP alloys in the red spectral range have been widely implemented for applications including solar cells [12] and electrically-pumped LEDs [13], because they offer high absorption in the blue spectral range (thus could be made thinner than 1μm and still absorb all the pump light), high IQE [14] and better photostability as shown in Table 1. They could therefore be a credible alternative to Q-dots in applications involving very high luminances (need for photostability) and compact integration scheme (need for CCL with thickness <1μm). However, most of the emitted light is guided inside the CCL due to their high refractive indices leading to low LEE and therefore low CE.

Table 1. Existing red color converters: main characteristics and challenges.

Color converter type	Blue absorption (absorption coefficient α)	Conversion efficiency limitation factor	Photostability	Ref.
Phosphors	Poor (α<0.01 μm^{-1})	η_{abs}	Photoluminescence quenching under high incident flux	[8]
QDs	Moderate (α~0.2 μm^{-1})	η_{abs}	Photoluminescence quenching under high incident flux	[9,10]
MQW (InGaP/ AlGaInP)	High (α >1μm^{-1})	*LEE*	Stable by nature (epilayer)	[4,10]

Besides, additional application-driven requirements have to be taken into account, in particular for microdisplays where the resolution is a key-element in the product development. Indeed, in such applications pixel lateral sizes can be less than 10 μm which means that not only most of the emitted light must be extracted out of the CCL, but also the extraction length (the lateral extent needed to extract most of the guided light) needs to be shorter than the pixel lateral size [15]. In addition, since these applications include systems with limited numerical apertures (NA), the CCL should also exhibit highly directional emission for efficient coupling to those optical systems [16]. From the integration point of view, there is also still a need to develop efficient bonding

Optics EXPRESS

methods to transfer the CCL on blue micro-LED arrays [10]. All the previously mentioned issues have to be circumvented in order for the inorganic MQW semiconductor CCL to become credible alternatives to Q-dots in microdisplay applications involving very high luminances and compact integration scheme. However, solutions to those key issues in microdisplay applications have not been reported yet.

Photonic crystals (PhCs), which are periodic dielectric perturbations at wavelength-scale, have already been widely applied to reach high LEE in high refractive-index materials [17–21]. Due to the coherent nature of their diffraction processes, they are also able to directly shape the light emission pattern of the CCL which would enhance the coupling to external optical systems with limited NA, avoiding the hitherto very bulky designs including light-collimating refractive lenses [22,23]. In addition, it has also been shown that they could exhibit strong interaction with guided Bloch modes when combined with thin-film devices, which could lead to very short extraction lengths [24]. Therefore, using PhCs could be an interesting route for solving the aforementioned issues.

In this paper, we investigate the design, fabrication and characterization of AlGaInP/InGaP MQW color converters exhibiting high light extraction within short extraction lengths and highly directional emission. The paper is organized as follows. Section 2 outlines the fabrication process with a successful oxide-mediated direct bonding of the CCL tested on a transparent substrate, while section 3 defines a FoM to assess the coupling of the emission from the CCL to external optical systems with limited NA. The experimental results are analyzed in section 4, highlighting some key design features and setting some design guidelines for such structures.

2. Device fabrication

The AlGaInP epitaxial structure to bond on a transparent substrate is depicted in Table 2. It is an epi-layer grown lattice matched on a 3-inch diameter GaAs substrate. The measured emission peak wavelength is ~640nm and the full width at half-maximum (FWHM) is ~20 nm. Layers 0, 1, 2 and 3 will be removed in the integration process.

Table 2. III-V epitaxial growth layer structure and characteristics

Layer	Material	Thickness	Refractive indices at λ=640nm
0: Substrate	GaAs	625 μm	
1: Buffer layer	U-GaAs	200 nm	
2: Etch-stop layer	U-InGaP	300 nm	
3: Sacrificial layer	U-GaAs	50 nm	
4: Cladding	U-$(Al_{x2}Ga_{1-x2})_{0.52}In_{0.48}P$	200 nm	n=3.4
5: MQW barrier	U-$(Al_{x1}Ga_{1-x1})_{0.52}In_{0.48}P$	70 nm	n=3.44
6: MQW region	4×U-$In_yGa_{1-y}P$/ 5×U-$(Al_{x1}Ga_{1-x1})_{0.52}In_{0.48}P$	4.4 nm/ 8.7 nm	$n_{average}$=3.49
7: MQW barrier	U-$(Al_{x1}Ga_{1-x1})_{0.52}In_{0.48}P$	70 nm	n=3.44
8: Cladding	U-$(Al_{x2}Ga_{1-x2})_{0.52}In_{0.48}P$	200 nm	n=3.4
9: Bonding interface	U-GaAs	20 nm	

We use oxide-mediated direct bonding to transfer this epi-layer onto a transparent substrate to fabricate a stand-alone color converter. A 10-nm-thick alumina film is deposited on the layer 9 of the epi-layer as an intermediate bonding layer by atomic layer deposition (ALD). Afterwards, a 200-mm transparent borosilicate substrate is encapsulated with 1.2 μm of SiO_2 deposited by PECVD, followed by chemical-mechanical polishing (CMP) which allows planarization of the wafer. Both the alumina film and the SiO_2 surfaces are activated through oxygen plasma and then

Optics EXPRESS

put in contact for molecular bonding. Afterwards, a 120 minutes post-bonding thermal annealing in nitrogen atmosphere at 300° C is performed to increase surface energy and therefore reinforce the bonding.

A scanning acoustic microscopy (SAM) image of the bonded epi-layer is displayed in Fig. 2(a). We can see that the epi-layer has been successfully transferred onto the substrate with a high bonding yield (>90%).

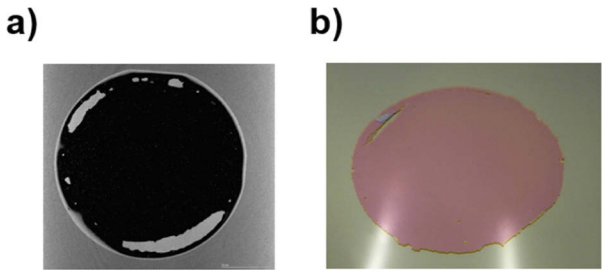

Fig. 2. a) Scanning acoustic microscopy (SAM) image of the bonded epi-layer before substrate removal. b) Picture of the bonded epi-layer (in red) after substrate and sacrificial layer removal.

Subsequently, the GaAs substrate and the sacrificial layers are removed by highly selective wet etching processes. GaAs substrate and GaAs buffer layer (layers 0 and 1) are both removed using NH_4OH / H_2O_2 /H_2O heated solution. Afterwards the InGaP etch-stop layer (layer 2) is removed using HCl / H_3PO_4 solution at ambient temperature, and then the last GaAs sacrificial layer (layer 3) is removed using the same NH_4OH-based chemical solution. All those wet etching processes are followed by a water rinse. In Fig. 2(b), a picture of the bonded epi-layer after substrate and sacrificial layer removal is displayed. The remaining epi-layer thickness is ~600nm.

The PhC patterns are fabricated using a well-established top-down pattern transfer method. First, a hard mask comprising a 150nm-thick PECVD SiN and a 10nm-thick PVD TiN has been deposited. After a 400nm-thick photoresist was spun on the hard mask, PhC patterns were defined using e-beam lithography and then transferred into the hard mask by chlorine-based and by fluorocarbon-based RIE for TiN and SiN layers respectively. After hard mask etching, the photoresist residues were stripped by O_2 plasma in nitrogen atmosphere. The PhC patterns were subsequently transferred into the epi-layer. The PhC pattern transfer was performed using chlorine-based ICP-RIE (Cl_2 /Ar). The hard mask was then removed by SF6-based RIE. A detailed flow chart of the device fabrication is provided in Supplement 1 (Note S1).

Two types of square lattices with varied opto-geometrical parameters have been fabricated: square lattice of air holes and square lattice of nanopillars. In the following, those lattices will be referred to as holes and pillars respectively. For each lattice type, different structures with different lattice periods have been fabricated: lattice periods from 400nm to 700nm with a step of 50nm. The lower and upper limits are to ensure respectively each of the guided modes supported by our CCL can be prone to diffraction into air and there can be enough diffractive elements in pixel sizes compatible with microdisplay applications (see Section 1). For a given lattice period, PhC structures with different lateral extents (lateral size in number of periods of the photonic crystals) have been fabricated: 3 periods, 5 periods, 10 periods, 25 periods, 50 periods and 100 periods. For all those fabricated structures, variants with two different etch depths have been fabricated: etch depths of ~188nm (~82nm above the MQW region) and ~288nm (PhC patterns etched in the active region). For each set of opto-geometrical parameters, arrays of structures ($>5\times5$) have been fabricated to perform statistical analyses on the wafer and rule out fabrication errors. In Fig. 3, SEM images of some of the fabricated structures are displayed.

Optics EXPRESS

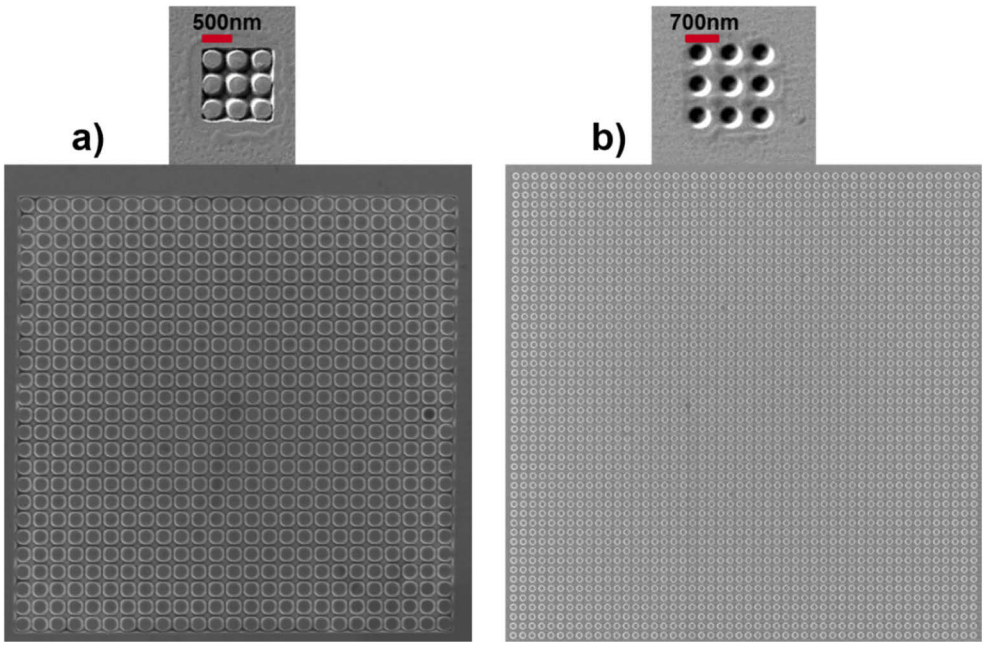

Fig. 3. Scanning electron microscopy images (SEM) of the fabricated structures. a) Square lattice of nanopillars with a lattice period a=500 nm and lateral extents of 3 periods (top) and 25 periods (bottom). b) Square lattice of air holes with a lattice period a=700 nm and lateral extents of 3 periods (top) and 50 periods (bottom).

3. Assessment of the directional light extraction efficiency

As mentioned in Section 1, in applications such as microdisplays where the emitting devices are to be coupled to external optical systems with limited numerical apertures, common light extraction efficiency (LEE) is not enough anymore to assess performances. Indeed only part of the emitted light couples to the optical system and this quantity depends on both LEE and farfield emission pattern [16]. Therefore a new FoM needs to be defined taking into account both LEE and emission pattern. We call it directional light extraction efficiency (DLEE).

The integrated intensity emitted within the acceptance angle θ is calculated as:

$$P(\theta) = \int_{\theta'=0}^{\theta'=\theta} \int_{\varphi=0}^{\varphi=2\pi} I(\theta', \varphi) \sin(\theta') d\theta' d\varphi, \tag{2}$$

where I is the emitted intensity (integrated over the whole emission spectrum), θ is the acceptance angle (apex angle of the acceptance cone related to the numerical aperture by $NA = sin\ (\theta)$) and φ is the azimuthal angle.

In this framework, DLEE reads as:

$$DLEE(\theta) = \frac{P(\theta)}{P_{int}} = \frac{P(\theta)}{P(90°)} \times \frac{P(90°)}{P_{int}} = D(\theta) \times LEE, \tag{3}$$

where P_{int} is the emitted intensity inside the structure (in our case the CCL) and $D\ (\theta)$ is the directionality of the radiation patterns of the CCL which is angular-dependent [16]. For θ=90°, this definition corresponds to the common LEE. Generally speaking, it accounts for light extraction inside a cone whose apex angle is θ.

As mentioned before, PhC structures are implemented to circumvent the LEE limit in planar CCL. In the following, the directional light extraction efficiency enhancement is given by the ratio

Optics EXPRESS

between DLEE of PhC structures and DLEE of the unpatterned reference structures. It reads as:

$$\eta_{DLEE}(\theta) = \frac{DLEE_{PhC}(\theta)}{DLEE_{unpatterned}(\theta)} = \frac{P_{PhC}(\theta)}{P_{unpatterned}(\theta)}, \quad (4)$$

where $P_{unpatterned}$ *and* P_{PhC} refer to the emitted intensity in Eq. (2) for the reference and PhC structures respectively.

4. Results and discussions

4.1. Experimental details and methodology

For proof of principle demonstration of color conversion and to experimentally evaluate the DLEE enhancement factors as a function of the acceptance angle, micro-photoluminescence (μ-PL) measurements were performed with a LabRAM photoluminescence (PL) setup from HORIBA. The samples are those where PhC etch depth is ~188nm. A 514 nm Argon laser line (for green-to-red color conversion) was focused at normal incidence by a microscope objective (MO) called excitation objective on the top side of the PhC structures. PL signals from the samples were collected with the same excitation objective and dispersed by a spectrometer. The so-formed spectrum is then collected with a CCD camera. Different excitation objectives with different numerical apertures (NA) were used to evaluate the angular dependence of DLEE enhancement and their characteristics are given in Table 3.

Table 3. Characteristics of the excitation objectives for PL measurements.

Numerical aperture	Acceptance angle	Average excitation power	Spot sizes
0.9	~64°	0.0315 μW	~1 μm
0.75	~49°	0.0370 μW	~1 μm
0.6	~37°	0.0310 μW	~1 μm
0.5	~30°	0.0245 μW	~1 μm
0.25	~14°	0.64 μW	~10 μm

Those numerical apertures allow us to scan acceptance angles between 14° (low acceptance angle) and 64° (high acceptance angles where almost all the emitted light is collected). For a given structure (given lattice type, lattice period and lateral extent), PL spectra were collected with all the microscope objectives. For each microscope objective, reference spectra were also collected on unpatterned zones to evaluate photoluminescence enhancement by the photonic crystals. Blue PL with an excitation at 405 nm was also performed for blue-to-red color conversion, exhibiting similar results (Note S2 in Supplement 1).

Figure 4 displays some of the measured PL spectra for the MO with NA=0.9 and for 10-period structures. PL spectra of the unpatterned structures are also added for reference. Both PhC and reference structures exhibit spectra with similar Lorentzian shapes (emission peak at ~640nm, FWHM~20nm) with higher peak intensities for PhC structures. The PL gains from the PhC structures depend on their opto-geometrical parameters and this dependency will be investigated with the evaluation of the DLEE enhancement factors.

To properly evaluate the DLEE enhancement factors, the ratios between spectrally integrated PL signals for PhC structures and for the reference structures were calculated. For a given acceptance angle, it reads as:

$$\eta_{DLEE}(\theta) = \frac{P_{PhC}(\theta)}{P_{unpatterned}(\theta)} = \frac{\int_{550nm}^{750nm} I_{PhC}(\lambda)d\lambda}{\int_{550nm}^{750nm} I_{unpatterned}(\lambda)d\lambda}, \quad (5)$$

where I_{PhC} and $I_{unpatterned}$ are PL intensities collected by a microscope objective with an acceptance angle θ ($NA = sin\ (\theta)$), for PhC and reference structures respectively.

Optics EXPRESS

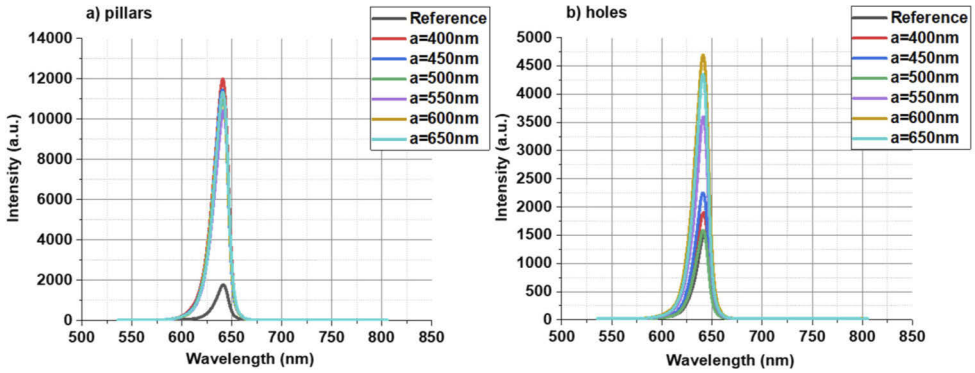

Fig. 4. Photoluminescence spectra from a laser excitation at 514 nm, for the microscope objective with NA=0.9, for 10-period structures and for different lattice periods. a) For square lattice of nanopillars. b) For square lattice of air holes. PL spectra of the unpatterned structures are also added.

4.2. Model to determine mean coupling strengths and extraction lengths

Figure 5 displays the experimental DLEE enhancement factors as a function of the lateral extent for the PhC structures with a lattice period of 600nm. The numerical aperture of the objective is 0.6. For a given lattice type (holes or pillars) and a given lattice period, the same acquisitions were performed with all numerical apertures to assess the device behavior as a function of the PhC lateral extent. Since arrays of structures of the same type (similar set of opto-geometrical parameters) have been fabricated (see Section 2), statistical analyses (not shown here for the sake of clarity) were also performed by randomly choosing four PhC structures for each measurement. The resulting standard deviations between measurements are very small (<0.05), which shows very good repeatability of the fabrication process in the 200mm clean room facilities and consistency of the measurements.

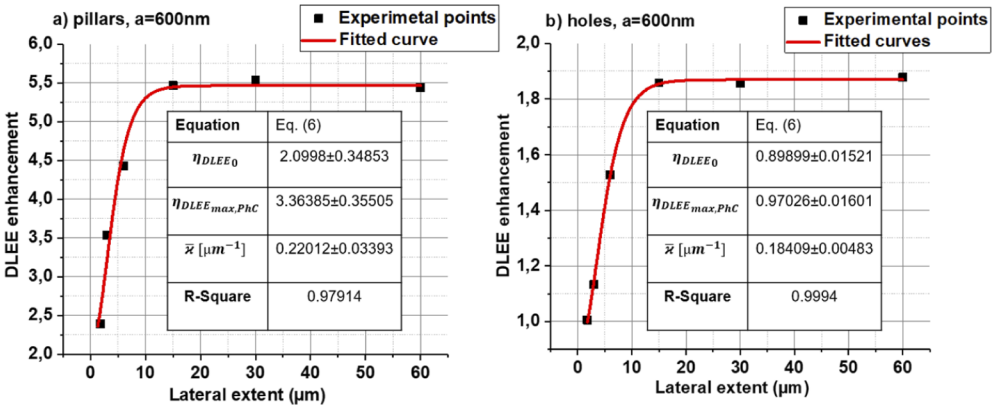

Fig. 5. Experimental DLEE enhancement as a function of the PhC lateral extent (in micrometers) for a) pillars and b) holes with a lattice period a=600 nm. NA=0.6. Experimental points are fitted with the proposed phenomenological model derived from the standard coupled-mode theory. Fit details are given in the inset.

We can observe that DLEE enhancement increases with the lateral extent of the PhC until it saturates at ~5.5 and ~1.9 for pillars and holes respectively.

Optics EXPRESS

The extraction length is a key parameter for designing high light extracting structures since it must be smaller than the lateral dimensions of the devices [15]. To determine the extraction lengths of the fabricated CCL, we propose a phenomenological model derived from the standard coupled-mode theory [25] which gives DLEE enhancement (noted η_{DLEE}) as a function of the PhC lateral extent L.

In the framework of our model, DLEE enhancement (for given lattice type, lattice period and acceptance angle) reads as:

$$\eta_{DLEE}(L) = \eta_{DLEE_0} + \eta_{DLEE_{max,PhC}} \times tanh^2(\bar{\kappa} \times L), \tag{6}$$

where η_{DLEE_0} accounts for direct light emission without guided Bloch-mode extraction (in this regime, e.g., for PhC structures with very short lateral extents, the PhC structure is equivalent to an homogeneous medium with a refractive index given by effective medium theory [26]), $\eta_{DLEE_{max,PhC}}$ accounts for the maximum light extraction of guided Bloch modes, the *tanh* function takes into account both propagating and counterpropagating guided Bloch modes, $\bar{\kappa}$ is the mean coupling strength (strength of the coupling between the guided Bloch modes inside the CCL and the radiated modes in the air) over all the diffracted modes for a given lattice type and lattice period and at a given acceptance angle and L is the PhC lateral extent.

This model was used to fit the measurements of DLEE enhancement factors as a function of the lateral extent of the PhC structures. Figure 5 shows the fitted curves with fit details in the inset. We repeated this fitting procedure with different microscope objectives to obtain the mean coupling strengths for each lattice type and each lattice period and at each acceptance angle. From those mean coupling strengths, we calculate the mean extraction lengths using the expression below [27]:

$$L_{extraction} = \frac{1}{\bar{\kappa}}. \tag{7}$$

Figure 6 displays the results:

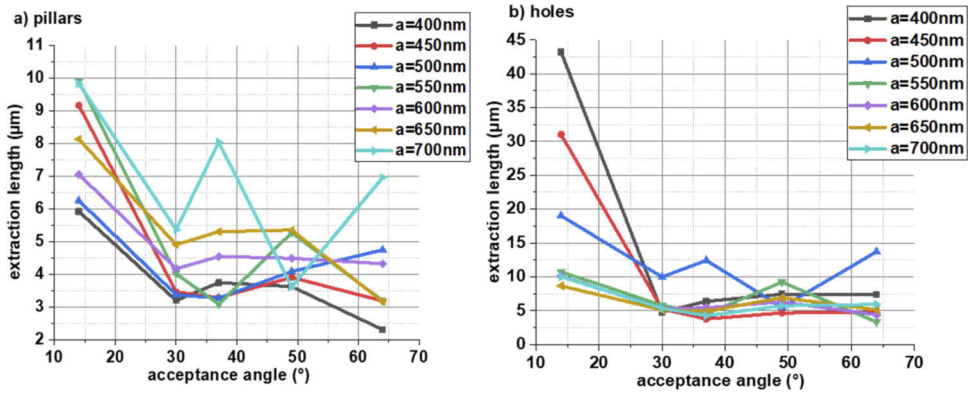

Fig. 6. Mean extraction lengths as a function of the acceptance angle for a) square lattice of nanopillars and b) square lattice of air holes for all the fabricated structures.

We notice that for both lattice types the extraction lengths strongly depend on the acceptance-angle. This results from the variations of the mean coupling strengths as a function of the acceptance angle. This dependency can be understood by conventional diffraction theory. Each of the guided Bloch modes supported by the multimode CCL has its own coupling strength depending on its overlap with the PhC patterns [27]. Since all those modes are diffracted to air within different angles according to Bragg law [28], the modes collected by the microscope objective are not the same when the acceptance angle changes. This results in strong variations

Optics EXPRESS

of mean coupling strengths as a function of the acceptance angle and therefore leading to strong variations of mean extraction lengths.

For pillars, the optimal lattice period is a=400nm offering the shortest extraction lengths (between 2 and 6 µm). In addition, we notice that for almost all lattice periods, there is an increase of the mean extraction lengths with decreasing acceptance angles: for a=400nm, there is almost a three-time increase from 64° to 14°.

For holes on the other hand, the optimal lattice period shifts to a higher lattice period (a=700nm) with extraction lengths between ~5µm at 64° and ~10µm at 14°. The dependency of extraction lengths on the acceptance angles are similar to those observed for pillars with longer extraction lengths obtained for holes. This suggests a higher overlap between the guided Bloch modes and the PhC structures for pillars resulting into stronger coupling to radiated modes and therefore shorter extraction lengths [24].

On a device point of view, there are two main conclusions from this analysis. On the one hand, it appears that the extraction lengths can be optimized (made shorter than the lengths of our devices) with a proper choice of the lattice period. On the other hand, for applications including optical systems with very low numerical apertures (low acceptance angles), CCL with longer lateral extents are needed.

4.3. Light extraction efficiency enhancement

From the previous analyses, it appeared that the extraction lengths for both lattice types are between ~2 and ~13µm at high acceptance angles (see Fig. 6). Therefore, the structures with a lateral extent of 100 periods can be considered "infinite" since their lateral extents are far longer than the extraction lengths in the range of our lattice periods. Figure 7 displays the LEE enhancement (Eq. (4) at high acceptance angles) factors for the structures with a lateral extent of 100 periods as a function of the lattice periods.

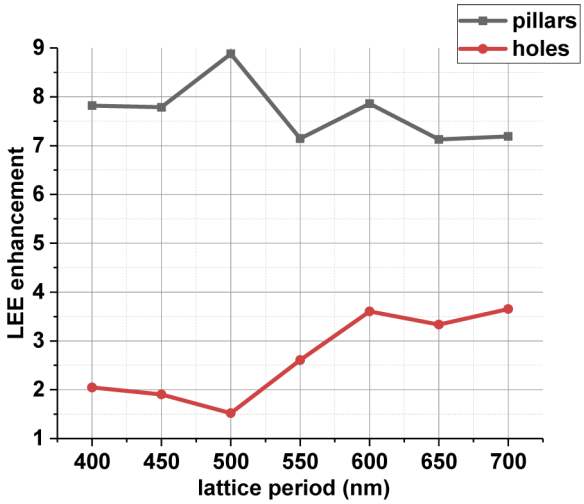

Fig. 7. Light extraction efficiency enhancement as a function of the lattice periods for holes and pillars with a lateral extent of 100 periods

For pillars, LEE enhancement only weakly depends on the lattice periods with high enhancement factors between 7 and 9 (a ~800% increase of light extraction compared to unpatterned references). On the other hand for holes, there is a slight increase of LEE enhancement with increasing lattice period from 2 for a=400nm to ~3.5 for a=700nm. Thus, the highest values of LEE enhancement are obtained for pillars.

Optics EXPRESS

Light extraction is generally in competition with absorption processes such as metal absorption or QW re-absorption. However, typical QW re-absorption lengths in our structures are 100µm [29], which is larger than our found extraction lengths and there is no metallic layer in our structures. We can therefore safely say that light extraction plays the preponderant role in our structures. Excitation-power dependent PL has also been performed (Note S3 in Supplement 1) to verify that the experimental enhancement factors do not vary with the excitation power which confirms the previous considerations. The remaining part of the light is diffracted toward the substrate, since PhC structures with large lattice periods (larger than second Bragg order which is around 200nm in our case) can open many diffraction channels toward the transparent substrate [30]. Therefore, the highest LEE enhancement obtained for pillars suggests that there is more light diffracted toward the substrate for holes than for pillars. This light can be redirected toward the top side using bottom reflectors.

Let us note that the high LEE enhancement factors (between 7 and 9) obtained for pillars are paired with very short extraction lengths (between 2 and 10µm) which makes them very relevant for achieving high conversion efficiency in devices with limited lateral extents such as in microdisplays.

4.4. Directional light extraction efficiency enhancement

As mentioned in section 3, LEE is not enough anymore to assess performances when dealing with systems with limited numerical apertures. Figure 8 displays DLEE enhancement for structures with a lateral extent of 100 periods (when all the guided light is extracted) as a function of the acceptance angles.

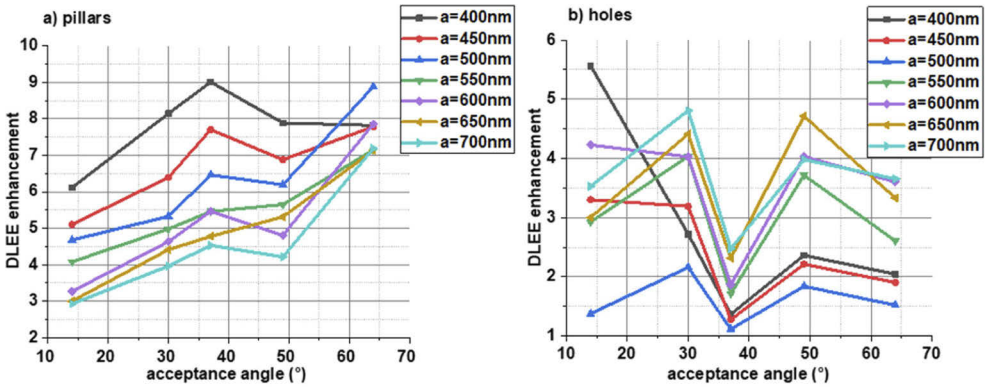

Fig. 8. Directional light extraction efficiency enhancement at saturation measured for different lattice periods as a function of the acceptance angle. a) For square lattice of nanopillars and b) square lattice of air holes with a lateral extent of 100 periods.

DLEE enhancement takes into account both LEE (not angular-dependent but lattice-period dependent) and directionality of the emission patterns (angular- and lattice-period-dependent) as described in section 3. Since the radiation patterns from our CCL can exhibit strongly intricate shapes due to the multimode nature of the CCL (see Note S4 in Supplement 1), DLEE enhancement depends on the acceptance angle as we can see in Fig. 8.

At high acceptance angles, DLEE enhancement corresponds to LEE enhancement. Therefore, for pillars, DLEE enhancement only weakly depends on lattice periods at high acceptance angles as seen previously. However, DLEE enhancement becomes lattice-period dependent for decreasing acceptance angles, which suggests strong variations of the emission pattern [31]. The optimal lattice period for pillars is a=400nm offering at the same time high DLEE enhancement

Optics EXPRESS

factors at all the measured acceptance angles (from ~8 at 64° to ~6 at 14°) and the shortest extraction lengths (see Section 4.2).

For holes on the other hand, the optimal lattice period clearly depends on the acceptance angle with a shift to lower lattice periods for decreasing acceptance angle, which suggests stronger variations of the emission pattern than for pillars. Particularly, for a=400nm and a=450nm the DLEE enhancement factors go from ~2 at 64° to ~5.5 and ~3 respectively. The highest DLEE enhancement factors for the measured angles are obtained for a=400nm at low acceptance angle (~5.5 at 14°) and for a=700 nm at high acceptance angles (~4 at 64°).

It thus appears that the coupling to an external optical system with a limited numerical aperture can be optimized by correctly choosing the lattice type and the lattice periods. For our structures, pillars with a lattice period of 400nm is the optimum since their offer high DLEE enhancement and the shortest extraction lengths in the range of the measured acceptance angles.

4.5. Identification of the different contributions in the measured LEE enhancement

Additional incoherent 3D-FDTD simulations in a pulsed regime were performed to evaluate light extraction efficiency for some of the fabricated structures to better understand our results. To perform those simulations, we use commercially available software (FullWAVE and LED Utility from the Rsoft Design Suite) [32,33]. The lateral dimensions of the computation domain were fixed at 10 lattice periods for computing time issues and surrounded by perfectly matched layers (PML). The input spectrum is Gaussian-shaped with a center wavelength at 640nm and a FWHM of 20nm as in our PL measurements. The MQW region was represented by a source plane of 50 transverse electric (TE)-polarized dipoles in the middle of the CCL (see Table 2). Structural parameters of the PhC structures (lattice periods, etch depth ~188nm and filling factors) are the ones measured in our fabricated structures (provided in Table 4). As a reference, we also performed calculations for flat structures to evaluate LEE enhancement factors. Figure 9 displays the measured and simulated LEE enhancement factors for 10-period structures with varying lattice periods (see Note S4 in Supplement 1 for the corresponding azimuthal farfield radiation patterns).

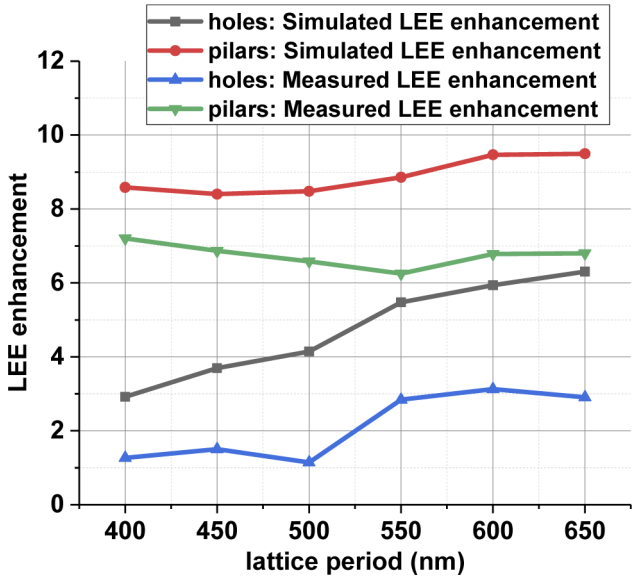

Fig. 9. Measured and simulated LEE enhancement for PhC structures with a lateral extent of 10 periods.

Optics EXPRESS

Table 4. Measured structural parameters of the fabricated PhC structures

	Diameter		Spacing		Air filling factor	
a	holes	pillars	holes	pillars	holes	pillars
400nm	159nm	236nm	241nm	164nm	12%	73%
450nm	199nm	271nm	251nm	179nm	15%	71%
500nm	237nm	343nm	263nm	157nm	18%	63%
550nm	331nm	397nm	219nm	153nm	28%	59%
600nm	368nm	446nm	232nm	154nm	30%	57%
650nm	412nm	491nm	238nm	159nm	32%	55%
700nm	462nm	534nm	238nm	166nm	34%	54%

For pillars, both measured and simulated LEE enhancement only weakly depend on the lattice periods whereas for holes both measured and simulated LEE enhancement increase for increasing lattice period. 3D-FDTD is therefore in agreement with our measurements, which supports our previous analysis. However measured LEE enhancement factors are lower than the simulated ones (e.g., ~1 and ~4 respectively measured and simulated for holes with a lattice period of 500nm) which means there are other contributions that tend to decrease the measured enhancement factors.

Let us recall that the measured enhancement factors correspond to the conversion efficiency which is the product of light absorption efficiency, IQE and LEE as in Eq. (1). Therefore light absorption efficiency and IQE need to be separately investigated. For light absorption efficiency, we performed RCWA simulations (Note S5 in Supplement 1) showing that the PhCs enhance light absorption by factors between ~1.4 and ~1, which is clearly not responsible of the discrepancies in Fig. 9.

Quantitative determination of the IQE would require further extensive studies and experiments that are out of the scope of the present discussion [34]. Instead, we conducted time-resolved PL measurements (TRPL) to estimate the decay lifetime of the PhC structures compared to the reference structures. The measurements were conducted using a picosecond laser diode head with a wavelength of excitation of 376 nm, a FWHM of 50 ps with a repetition rate of 5 MHz for pulsed operation. TRPL signals were collected using a solid state photon counting detector that counts photons emitted at the peak wavelength ~640 nm. Since the excitation wavelength is in the UV range, carrier dynamics and thermalisation processes are not the same as in our experiments [35], however it could give a good insight of IQE variations.

The IQE is given by the ratio of probabilities of radiative ($1/\tau_R$) and total recombination ($1/\tau=1/\tau_{R+}1/\tau_{NR}$), where τ_R and τ_{NR} are the radiative and non-radiative recombination lifetimes [36]. Since the radiative lifetimes do not vary between the PhC structures and the reference structures in this case, the ratios of the total lifetimes for PhC and unpatterned structures directly give the IQE ratios between those two.

Figure 10 displays the TRPL results. Figure 10(a) shows one of the TRPL transient curves with the fitting function. All the transient curves were fit with a single exponential decay function, given by $I_{TRPL}=A\times exp(-t/\tau)$, where A is the amplitude and τ the total recombination lifetime as in [37]. Figure 10(b) displays the IQE ratios for holes and pillars as a function of the lattice period for the two different etch depths.

Depending on the lattice periods and the etch depth, we can observe a decrease of the IQE of the PhC structures compared to the reference structures. For instance, for pillars with a=400nm and an etch depth of 188nm the IQE of the reference structure is almost two times higher than the one of the PhC structures. We also notice that when PhC patterns are etched in the active region (etch depth ~288nm in Fig. 10(b)), the IQE of the PhC structures strongly decreases (almost

Optics EXPRESS

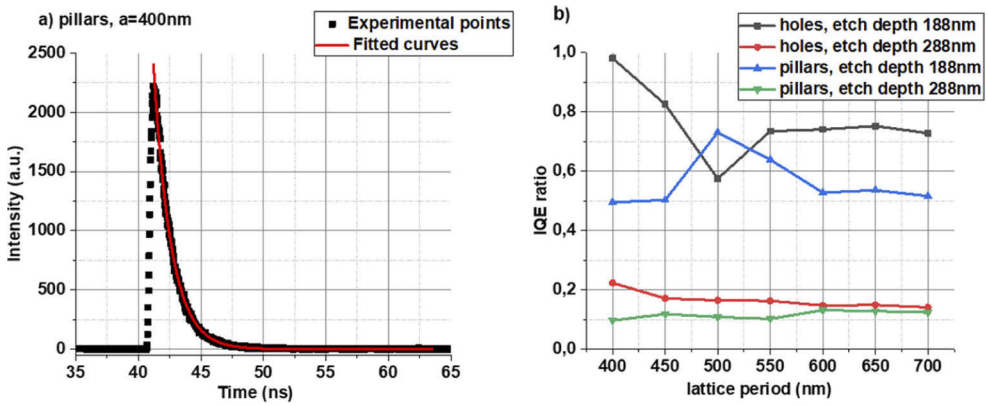

Fig. 10. TRPL results for two etch depths as a function of the lattice period. a) Transient curve for pillars with a=400 nm. b) IQE ratios between PhC and unpatterned structures.

five times lower compared to etch depth ~188nm). For the samples with etch depth ~288nm, measured DLEE enhancement factors (not shown here) are less than 1, meaning that the IQE decrease is so strong that PL gains cannot be observed and PhC patterns actually decrease the PL intensity. This is a result of the large number of surface defect states created at the sidewall of the photonic crystals combined with high surface recombination velocities and high carrier diffusion lengths in AlGaInP [37]. It thus appears that to fabricate highly efficient color converters with the InGaP/AlGaInP material system, the active region should not be etched at all unless efficient passivation techniques are performed [37].

It should however be noted that in our experiments, the incoming excitation light is focused on the top side of the PhC structures, therefore carrier generation mostly occurs in the etched regions. For example in the sample with etch depth ~188nm and with a pump on the bottom side of the CCL, we could expect that carrier generation would preferentially happen in the unetched zones, which would then mitigate the IQE ratios in Fig. 10. Still, the measurements of Fig. 10 are an evidence that IQE decrease is mostly responsible of the discrepancies between simulated and measured LEE enhancement factors in Fig. 9.

5. Conclusion

We have reported on the design, fabrication and characterization of AlGaInP/InGaP MQW color converters exhibiting high light extraction efficiency within short extraction lengths and highly directional emission. The color converters have been successfully transferred onto a transparent substrate to fabricate stand-alone color converters. Photonic crystals with different opto-geometrical parameters were fabricated.

Room-temperature photoluminescence was used as proof-of-principle for color conversion. Blue-to-red and green-to-red color conversions have been successfully demonstrated with enhanced conversion efficiencies (through enhanced LEE) and directional light emission. In all the fabricated structures, quasi-perfect light out-coupling (light extraction) has been demonstrated showing that light extraction is not an issue anymore. Besides, a model derived from the standard coupled-mode theory has been proposed showing very high coupling between the guided Bloch modes and the PhC patterns, which results in short extraction lengths (between 2 and 6μm for the best structures) making them compatible with micro-sized devices. It has also been shown that directional light emission within low angles leads to longer extraction lengths which sets some design rules regarding the lateral extent of devices based on color conversion. 3D-FDTD simulations coupled to TRPL analyses are consistent with the results while highlighting the

Optics EXPRESS

fact that AlGaInP based color converters can experience a rapid decrease of their conversion efficiencies if carrier generation happens in etched regions, unless efficient passivation techniques are performed.

The best fabricated color converters are those based on square lattice of nanopillars with a lattice period of 400nm. They exhibit the highest light extraction efficiency enhancement factors (a ~800% increase compared to the unpatterned reference structures) within the shortest extraction lengths (between 2 and 6µm depending on the acceptance angle). Those structures also exhibit a very directional light emission, allowing efficient coupling to external optical systems with limited numerical apertures which is of major importance for applications such as microdisplays.

We believe that all the design guidelines set through our analyses in this work make inorganic MQW epi-layer color converters credible alternatives to existing color converters and could pave the way for the use of color conversion instead of native color to achieve full color microdisplays on a single wafer.

Current and future works are mainly focused on investigating all the steps required for the implementation of the herein fabricated color converters on blue or green micro-LED arrays.

Funding. Horizon 2020 Framework Programme (755497).

Acknowledgments. The authors would like to thank C. Licitra for his help on device characterization and E.Quesnel for insightful discussions.

Disclosures. The authors declare no conflicts of interest.

Data availability. Data underlying the results presented in this paper are not publicly available at this time but may be obtained from the authors upon reasonable request.

Supplemental document. See Supplement 1 for supporting content.

References

1. S. Li, L. Wang, N. Hirosaki, and R.-J. Xie, "Color Conversion Materials for High-Brightness Laser-Driven Solid-State Lighting," Laser Photonics Rev. **12**(12), 1800173 (2018).
2. C. Li, H. Kimura, T. Saito, K. Sakurai, B. Wei, M. Ichikawa, and Y. Taniguchi, "Study of color-conversion-materials in chromatic-stability white organic light-emitting diodes," Opt. Express **15**(22), 14422–14430 (2007).
3. I. Rreza, H. Yang, L. Hamachi, M. Campos, T. Hull, J. Treadway, J. Kurtin, E. M. Chan, and J. S. Owen, "Performance of Spherical Quantum Well Down Converters in Solid State Lighting," ACS Appl. Mater. Interfaces **13**(10), 12191–12197 (2021).
4. J. M. M. Santos, B. E. Jones, P. J. Schlosser, S. Watson, J. Herrnsdorf, B. Guilhabert, J. J. D. McKendry, J. D. Jesus, T. A. Garcia, M. C. Tamargo, A. E. Kelly, J. E. Hastie, N. Laurand, and M. D. Dawson, "Hybrid GaN LED with capillary-bonded II–VI MQW color-converting membrane for visible light communications," Semicond. Sci. Technol. **30**(3), 035012 (2015).
5. E. Quesnel, A. Suhm, M. Consonni, M. Reymermier, G. Lorin, C. Laugier, M. Tournaire, P. L. Maitre, A. Lagrange, B. Racine, M. D'Amico, and E. Cao, "Experimental and theoretical investigation of 2D nanoplatelet-based conversion layers for color LED microdisplays," Opt. Express **29**(13), 20498–20513 (2021).
6. J. H. Oh, K.-H. Lee, H. C. Yoon, H. Yang, and Y. R. Do, "Color-by-blue display using blue quantum dot light-emitting diodes and green/red color converting phosphors," Opt. Express **22**(S2), A511–A520 (2014).
7. C.-M. Kang, J.-Y. Lee, D.-J. Kong, J.-P. Shim, S. Kim, S.-H. Mun, S.-Y. Choi, M.-D. Park, J. Kim, and D.-S. Lee, "Hybrid Full-Color Inorganic Light-Emitting Diodes Integrated on a Single Wafer Using Selective Area Growth and Adhesive Bonding," ACS Photonics **5**(11), 4413–4422 (2018).
8. C. C. Lin and R.-S. Liu, "Advances in Phosphors for Light-emitting Diodes," J. Phys. Chem. Lett. **2**(11), 1268–1277 (2011).
9. J. Osinski and P. Palomaki, "4-5: Quantum Dot Design Criteria for Color Conversion in MicroLED Displays," SID Symposium Digest of Technical Papers **50**(1), 34–37 (2019).
10. E. Quesnel, A. Lagrange, M. Vigier, M. Consonni, M. Tournaire, V. L. Marchand, A. Suhm, P. Demars, J.-C. Pillet, B. B. Bakir, N. Olivier, E. Feltin, J. M. Lamy, M. D'Amico, E. Cao, G. Haas, L. Charrier, and P. Coni, "Dimensioning a full color LED microdisplay for augmented reality headset in a very bright environment," J. Soc. Inf. Disp. **29**(1), 3–16 (2021).
11. S. Han, C. Xu, H. Li, S. Liu, H. Xu, Y. Zhu, A. Fang, and X. Wang, "AlGaInP-based Micro-LED array with enhanced optoelectrical properties," Opt. Mater. **114**, 110860 (2021).
12. J. S. Cheong, A. N. A. P. Baharuddin, J. S. Ng, A. B. Krysa, and J. P. R. David, "Absorption coefficients in AlGaInP lattice-matched to GaAs," Solar Energy Materials and Solar Cells **164**, 28–31 (2017).

Optics EXPRESS

13. Y. Wang, B. Wang, W. A. Sasangka, S. Bao, Y. Zhang, H. V. Demir, J. Michel, K. E. K. Lee, S. F. Yoon, E. A. Fitzgerald, C. S. Tan, and K. H. Lee, "High-performance AlGaInP light-emitting diodes integrated on silicon through a superior quality germanium-on-insulator," Photon. Res. **6**, 290–295 (2018).
14. Th. Gessmann and E. F. Schubert, "High-efficiency AlGaInP light-emitting diodes for solid-state lighting applications," J. Appl. Phys. **95**(5), 2203–2216 (2004).
15. T. A. Truong, L. M. Campos, E. Matioli, I. Meinel, C. J. Hawker, C. Weisbuch, and P. M. Petroff, "Light extraction from GaN-based light emitting diode structures with a noninvasive two-dimensional photonic crystal," Appl. Phys. Lett. **94**(2), 023101 (2009).
16. K. Bergenek, C. Wiesmann, H. Zull, C. Rumbolz, R. Wirth, N. Linder, K. Streubel, and T. F. Krauss, "Beam-shaping properties of InGaN thin-film micro-cavity light-emitting diodes with photonic crystals," in *Light-Emitting Diodes: Materials, Devices, and Applications for Solid State Lighting XIII* (International Society for Optics and Photonics, 2009), Vol. 7231, p. 72310C.
17. M. Boroditsky, T. F. Krauss, R. Coccioli, R. Vrijen, R. Bhat, and E. Yablonovitch, "Light extraction from optically pumped light-emitting diode by thin-slab photonic crystals," Appl. Phys. Lett. **75**(8), 1036–1038 (1999).
18. X. Tang, X. Tang, X. Tang, L. Han, L. Han, L. Han, Z. Ma, Z. Ma, Z. Ma, Z. Deng, Z. Deng, Z. Deng, Y. Jiang, Y. Jiang, W. Wang, W. Wang, W. Wang, H. Chen, H. Chen, H. Chen, C. Du, C. Du, C. Du, C. Du, H. Jia, H. Jia, H. Jia, and H. Jia, "Enhanced light extraction from AlGaInP-based red light-emitting diodes with photonic crystals," Opt. Express **29**(4), 5993–5999 (2021).
19. R. Lin, S. V. Galan, H. Sun, Y. Hu, M. S. Alias, B. Janjua, T. K. Ng, B. S. Ooi, and X. Li, "Tapering-induced enhancement of light extraction efficiency of nanowire deep ultraviolet LED by theoretical simulations," Photon. Res. **6**(5), 457–462 (2018).
20. B. Jain, R. T. Velpula, M. Tumuna, H. Q. T. Bui, J. Jude, T. T. Pham, T. T. Pham, T. van Le, T. van Le, A. V. Hoang, A. V. Hoang, R. Wang, and H. P. T. Nguyen, "Enhancing the light extraction efficiency of AlInN nanowire ultraviolet light-emitting diodes with photonic crystal structures," Opt. Express **28**(15), 22908–22918 (2020).
21. X. Liu, K. Mashooq, T. Szkopek, and Z. Mi, "Improving the Efficiency of Transverse Magnetic Polarized Emission from AlGaN Based LEDs by Using Nanowire Photonic Crystal," IEEE Photonics J. **10**(4), 1–11 (2018).
22. J. J. Wierer, A. David, and M. M. Megens, "III-nitride photonic-crystal light-emitting diodes with high extraction efficiency," Nature Photon **3**(3), 163–169 (2009).
23. X. Fu, Y. Mehta, Y.-A. Chen, L. Lei, L. Zhu, N. Barange, Q. Dong, S. Yin, J. Mendes, S. He, R. Gogusetti, C.-H. Chang, and F. So, "Directional Polarized Light Emission from Thin-Film Light-Emitting Diodes," Adv. Mater. **33**(9), 2006801 (2021).
24. A. David, T. Fujii, B. Moran, S. Nakamura, S. P. DenBaars, C. Weisbuch, and H. Benisty, "Photonic crystal laser lift-off GaN light-emitting diodes," Appl. Phys. Lett. **88**(13), 133514 (2006).
25. L. A. Coldren, S. W. Corzine, and M. L. Mashanovitch, *Diode Lasers and Photonic Integrated Circuits*, 2nd Edition (Wiley–Blackwell, 2012), Chap. 6.
26. C. Wiesmann, K. Bergenek, N. Linder, and U. T. Schwarz, "Analysis of the emission characteristics of photonic crystal LEDs," in *Photonic Crystal Materials and Devices VIII* (International Society for Optics and Photonics, 2008), Vol. 6989, p. 69890L.
27. E. Matioli, B. Fleury, E. Rangel, E. Hu, J. Speck, and C. Weisbuch, "Measurement of extraction and absorption parameters in GaN-based photonic-crystal light-emitting diodes," J. Appl. Phys. **107**(5), 053114 (2010).
28. K. Bergenek, Ch. Wiesmann, R. Wirth, L. O'Faolain, N. Linder, K. Streubel, and T. F. Krauss, "Enhanced light extraction efficiency from AlGaInP thin-film light-emitting diodes with photonic crystals," Appl. Phys. Lett. **93**(4), 041105 (2008).
29. R. G. Baets, D. G. Delbeke, R. Bockstaele, and P. Bienstman, "Resonant-cavity light-emitting diodes: a review," in *Light-Emitting Diodes: Research, Manufacturing, and Applications VII* (International Society for Optics and Photonics, 2003), Vol. 4996, pp. 74–86.
30. A. David, H. Benisty, and C. Weisbuch, "Photonic crystal light-emitting sources," Rep. Prog. Phys. **75**(12), 126501 (2012).
31. K. Bergenek, C. Wiesmann, H. Zull, C. Rumbolz, R. Wirth, N. Linder, K. Streubel, and T. F. Krauss, "Strong High Order Diffraction of Guided Modes in Micro-Cavity Light-Emitting Diodes With Hexagonal Photonic Crystals," IEEE J. Quantum Electron. **45**(12), 1517–1523 (2009).
32. G. J. Lee and Y. M. Song, "Theoretical analysis and experiment of subwavelength structure-integrated red AlGaInP light-emitting diodes for uniform field distribution and enhanced light extraction efficiency," AIP Adv. **6**(3), 035104 (2016).
33. P. Zhao and H. Zhao, "Analysis of light extraction efficiency enhancement for thin-film-flip-chip InGaN quantum wells light-emitting diodes with GaN micro-domes," Opt. Express **20**(S5), A765–A776 (2012).
34. P. Altieri, A. Jaeger, R. Windisch, N. Linder, P. Stauss, R. Oberschmid, and K. Streubel, "Internal quantum efficiency of high-brightness AlGaInP light-emitting devices," J. Appl. Phys. **98**(8), 086101 (2005).
35. E. E. Nyein, U. Hommerich, C. Munasinghe, A. J. Steckl, and J. M. Zavada, "Excitation-Wavelength Dependent and Time-Resolved Photoluminescence Studies of Europium Doped GaN Grown by Interrupted Growth Epitaxy (IGE)," MRS Online Proceedings Library **866**, 1–6 (2004).
36. E. F. Schubert, *Light-Emitting Diodes*, 3rd Edition (Cambridge University Press, 2018), Chap. 2.
37. Y. Boussadi, N. Rochat, J.-P. Barnes, B. B. Bakir, P. Ferrandis, B. Masenelli, and C. Licitra, "Investigation of sidewall damage induced by reactive ion etching on AlGaInP MESA for micro-LED application," Journal of Luminescence **234**, 117937 (2021).